LINKING EXPERIMENTAL CAPILLARY PRESSURE-SATURATION DATA WITH LATTICE BOLTZMANN SIMULATIONS

M.G. SCHAAP[1,2], B.S.B. CHRISTENSEN[3], M.L. PORTER[4], D. WILDENSCHILD[4]

[1] *University of California, Department of Environmental Sciences, Riverside, USA.*
[2] *Office at: GEBJ Salinity Laboratory USDA-ARS, Riverside, 450 W. Big Springs Road, Riverside, CA 92507, USA, mschaap@ucr.edu*
[3] *Institute of Environment & Resources, Technical University of Denmark, DK-2800 Kongens Lyngby, Denmark*
[4] *Department of Geosciences, Oregon State University, Corvallis, OR 97331, USA*

ABSTRACT

This study provides the basic steps needed to use a Shan-Chen (S-C) type two-component Lattice Boltzman model for simulating wetting – nonwetting displacement experiments and pressure saturation curves. The experimental data consist of CMT observations several Sotrol-water displacements inside a glass bead system with a resolution of 17 microns. An analysis of dimensionless quantities shows that capillary forces dominate over viscous, gravitational and inertial forces. The study also provides a procedure for simultaneously determining the surface tension and the contact angle. Subsequent simulations in observed porous media with a total of 2e7 voxels show that pressure-saturation equilibria are reached in 1e5 to >4e5 iterations. Preliminary results show that saturation profiles are non-uniform, with much drier conditions near the non-wetting boundary and wetter conditions near the wetting boundary. Both effects are probably related to limitations in percolation and, possibly, spatial correlation of fluid interfaces.

1. INTRODUCTION

Recent advances in observational and computational techniques have facilitated the study of fluid dynamics and interfacial geometry in porous media. Within some experimental limitations, computed tomography X-ray (CMT) and magnetic resonance imaging (MRI) are now able to accurately map the 3D structure of porous geometries. Computational advances largely concern Lattice Boltzmann (LB) method that has been shown to be useful in simulating microscale flow and interfacial phenomena in porous media.

The goal of this presentation is to provide insight into what is needed to make a link between 3D experimental observations of interfacial geometry and LB simulations. The analyses are partly performed on idealized systems and finally applied to large scale simulations of the real physical systems.

2. METHODS

2.1 Lattice Boltzmann model summary.

The basis of our LB model is the two component model proposed by Shan-Chen [1993, 1994] and modified by Martys and Chen [1996]. For reasons of brevity this model will not be discussed in detail, only the fluid-fluid (cohesion) and fluid-solid (adhesion) interactions will be given here. Fluid cohesion, causing surface tension, and fluid adhesion, which defines the wettability and contact angle, are implemented in the Shan-Chen model by modifying the microscale momenta of the fluids, leading to an alteration in the velocity distributions at the scale of LB nodes. Fluid cohesion forces are defined by

$$F_{c,\alpha} = -n_\alpha(\boldsymbol{x}) \sum_i^{19} G_{c,\alpha,\alpha',i} n_{\alpha'}(\boldsymbol{x}+\boldsymbol{e_i})\boldsymbol{e_i} \tag{1}$$

where $n(\mathbf{x})$ is the number density at location $\mathbf{x}$ (x,y,z), and $\mathbf{e}$ is the D3Q19 coordinate system that indicates the relative position of nearest and next-nearest neighbors; i indicates an individual LB link. The variables α and α' denote the two different fluid components. Fluid miscibility is set by the parameter interaction strength parameter $G_{c,\alpha\alpha',i}$ that is equal to $2G_c$ for nearest neighbor links, but G_c for more distant next nearest neighbor links [Martys and Chen, 1996]. The value of G_c should be positive and identical for both fluid components. Increasing G_c beyond a critical value will lead to progressively purer component mixtures. At some point, however, numerical instabilities are encountered because of negative number densities.

Pressure is determined by both fluids *and* their interaction. The following expression holds for a mixture of ideal gases in the limit of very weak interactions [Shan and Doolen, 1996]

$$P = \frac{1}{3}[n_\alpha(\boldsymbol{x})+n_{\alpha'}(\boldsymbol{x})]+12G_c n_\alpha n_{\alpha'} \tag{2}$$

capillary pressure, P_c, is defined as the pressure difference of the non-wetting and the wetting phases.

Adhesive forces between a solid phase and a fluid component are determined by the presence of solids in neighbouring nodes that surround a fluid node.

$$F_{a,\alpha} = -n(\boldsymbol{x}) \sum_i^{19} G_{a,\alpha} s(\boldsymbol{x}+\boldsymbol{e_i})\boldsymbol{e_i} \tag{3}$$

here $s(\mathbf{x}+\mathbf{e_i})$ is 1 for a solid and 0 for a pore. G_a controls the interaction strength and wetting properties of the fluids. To simulate systems of variable wettability, a positive interaction strength would be used for non-wetting fluid and a negative for wetting fluid. By changing the interaction strength, different contact angles between a fluid-fluid and fluid-solid interface can be obtained.

2.2 Experimental system.

Here we very briefly summarize how the experimental data was obtained and describe the physical properties of the system. Detailed descriptions of the experiments and methods can be found in Wildenschild et al. [2002] and Culligan et al. [2004, 2005].

The CMT experiments used to characterize the system of interest were conducted at the GeoSoilEnviro Consortium for Advanced Radiation sources (GSECARS) bending magnet beamline, Advanced Photon Source, Argonne National Laboratory. The resulting

experimental data consists of three-dimensional pore-scale images of oil and water displacement in a glass bead porous medium. The diameter of the soda lime glass beads range between 0.6-1.4 mm. Water was used as wetting phase and Soltrol 220 (a light non-aqueous phase liquid, LNAPL) as non-wetting phase. The top and bottom of the sample were connected to oil and water reservoirs, respectively. A vertical section of 6 mm of the sample was imaged with a resolution of 17 microns per voxel. After image analysis various properties of the system such as fluid saturations and fluid-fluid interfacial areas were quantified from the image data.

The properties of the experimental system are given in Table 2. The properties of Soltrol 220 have been reported differently in the literature and often it is unclear which temperature the measurements were made at. The Soltrol properties in Table 2 are from Kechavarzi et al. [2000], valid for a temperature of 23 °C, which corresponds well with the ambient temperature at the experimental site.

The wetting properties for the oil and water used in the experiment have been examined by measuring the contact angle. Due to some problems with the measurement it was difficult to precisely determine the contact angle, yet based on results an estimate of a zero degree contact angle was considered plausible. This means that the water almost perfectly wets the glass beads and therefore oil is considered the non-wetting phase.

TABLE 1. Properties of the experimental system.

Property	Value	Units
Porosity, Φ	0.34	
Resolution (voxel size)	$1.7 \cdot 10^{-5}$	m
Sample height (imaged section)	$6.1 \cdot 10^{-3}$ (360)	m (voxels)
Sample diameter	$6.9 \cdot 10^{-3}$ (405)	m (voxels)
Glass bead density, ρ_{bead}	$2.5 \cdot 10^3$	kg/m^3
Surface Area	$3.33 \cdot 10^3$	m/m^2
Characteristic pore radius, R	$2.07 \cdot 10^{-4}$	m
Water density, ρ_w	$1 \cdot 10^3$	kg/m^3
Soltrol density, ρ_o	$0.79 \cdot 10^3$	kg/m^3
Water dynamic viscosity, μ_w	$1.00 \cdot 10^{-3}$	Pa s
Soltrol dynamic viscosity, μ_o	$4.82 \cdot 10^{-3}$	Pa s
Soltrol-water interfacial tension, σ_{o-w}	0.042	N/m
Soltrol-water-glass contact angle, θ	0	degrees
Flow rate (Darcy velocity) range, v_w	$3.6 \cdot 10^{-6}$ to $2.2 \cdot 10^{-5}$	m/s
Gravitational acceleration, g	9.8	m/s^2
Capillary pressure range, p_c	0 to 1100	Pa
Water saturation range, S_w	0.1 to 0.9	-

2.3 System simplification.

A common way to evaluate the forces controlling the experimental flow system is to determine the Bond number (*Bo*, the ratio of gravitational and interfacial forces), the capillary number (*Ca*, the ratio of viscous and capillary forces), and the Reynolds number (*Re*, the ratio

of inertial and viscous forces). Ranges of these numbers for our experimental system are given in Table 2. Based on the magnitude of the Bond number we can conclude that capillary forces acting on the fluids are much larger than the gravitational forces (e.g buoyancy). In addition, the height of the imaged section of sample is only 6 mm, thus making the gravitational potential difference between top and bottom much smaller than the pressure range over which the experiment was conducted. We can therefore make the simplifying assumption that gravitational forces can be neglected in the LB simulations. Similarly, the Capillary number shows that viscous forces are negligible compared to capillary forces while the Reynolds number shows that inertial forces are much smaller than viscous forces. These dimensionless quantities confirm that capillary forces dominate the system as also found by Culligan et al. [2005]. The above analysis allows for a substantial system simplification for subsequent LB modeling as viscous, gravitational, and inertial forces can be omitted. However, we must still define density, interfacial tension, contact angle and the space scaling.

TABLE 2. Dimensionless numbers governing the oil-water experiments with the subscript x referring to oil or water.

Dimensionless characteristics		Min	Max
Bond number,	$Bo = g(\rho_w - \rho_o) R^2 / \sigma_{o-w}$		$2.09 \cdot 10^{-3}$
Capillary number,	$Ca = v_x \mu_x / \phi \sigma_{o-w}$	$2.52 \cdot 10^{-7}$	$7.43 \cdot 10^{-6}$
Reynolds number,	$Re = \rho_x v_x R / (\phi \mu_x)$	$3.58 \cdot 10^{-4}$	$1.34 \cdot 10^{-2}$

2.4   Space and pressure scaling

When relating physical space with the lattice space it is convenient to define Laplace's law in a reduced physical scale by dividing the physical capillary pressure with the physical surface tension. There is still space dimension, which can be removed by defining the space scale of the physical radius R_p as $h_p \cdot R_L$, where R_p and h_p are in physical units [m] and R_L is in lattice units (in our case $h = 17 \cdot 10^{-6}$ [m], Table 1). The same approach can be used for the lattice scale. By equating the lattice terms to the physical terms we can define an equation that provides the physical capillary pressure

$$P_{c,p} = \frac{\sigma_p P_{c,L}}{h_p \sigma_L} \quad [Pa] \tag{4}$$

In order to calculate the physical capillary pressure we need to know the resolution (h_p), the lattice capillary pressure, $P_{c,L}$, and the surface tension of the lattice and physical systems, σ_L and σ_p, respectively. All these values are known from the experiments or from numerical experiments in the next section.

2.5   Numerical Calibration

To set lattice interfacial tension and contact angle the fluid-fluid and fluid-solid parameters G_c and G_a must be derived empirically in numerical experiments. From eqns. 1 and 3 it is clear that both parameters effectively appear as a product with the number density, $n(\mathbf{x})$. Without going into detail here we set G_c at 0.025 and the sum of the number densities of both components, or total density ρ_i, at 2.0. Equivalent results are obtained for reasonable

combinations of G_c and ρ_i as long as $G_c \rho_i$=0.05. This particular value was chosen because larger values sometimes produced numerical instabilities, whereas smaller values resulted in insufficient separation of the wetting and non-wetting components.

Lattice surface tension and contact angle for 2D and 3D systems were obtained by enclosing equal masses of wetting fluid (blue) and a non-wetting fluid (red) in a closed capillary consisting of parallel walls in 2D and a square duct in 3D. The red fluid was placed in the middle of the capillary (cf. Figure 1) with blue on top and bottom. The parameter G_c was set at 0.025 while G_a was varied between 0 and 0.02. The simulations were carried out for different tube radii (3,4,5,9,14,19,29, and 39 in 2D and 3,4,5,9, 14 and 19 for 3D systems); the tube length was 160 pixels (320 for the simulations with 39-pixel radii). The simulations were run for 100,000 iterations.

The top row in Figure 1 shows that the contact angle changed from 90 degrees at G_a=0 (both fluids are neither wetting nor non-wetting) to zero at $G_a \sim 0.012$. At larger values of G_a the red non-wetting fluid detaches from the wall and an increasingly thicker film is formed. The lower row in Figure 1 shows the results at G_a=0.012 for all radii for which 2D simulations were carried out.
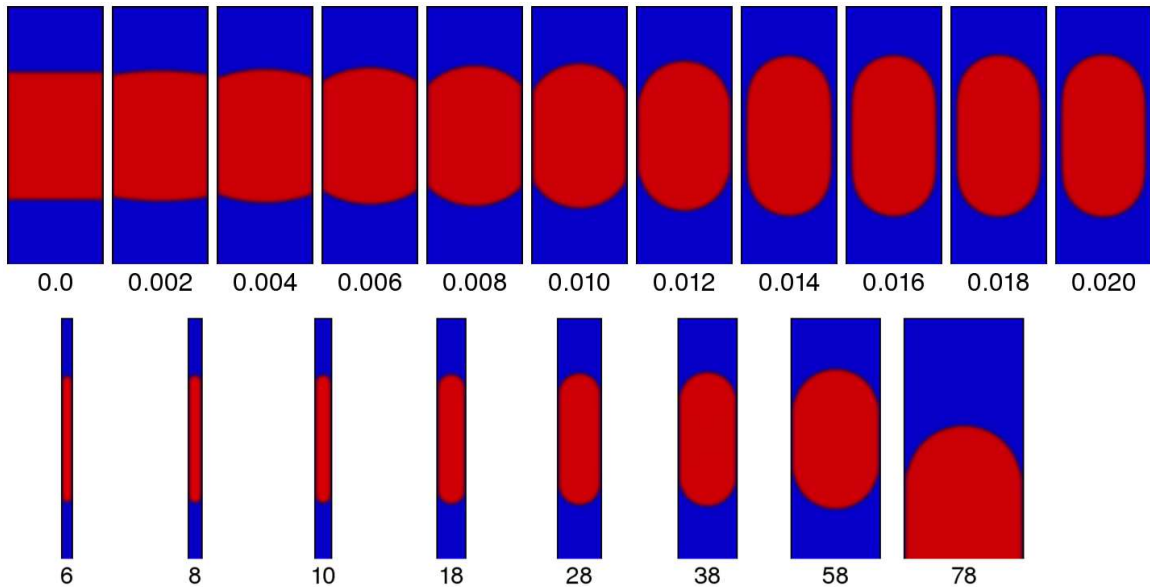

FIGURE 1. Tube simulations with enclosed wetting and non-wetting fluids. Top row show the formation of more intense curvature for a non-wetting bubble in a 2-D tube with a radius of 19 pixels for G_c=0.025 and G_a between 0 and 0.02. Bottom row shows results for G_a=0.012 for tubes with radii between 6 and 39 pixels (in the latter case only half the image is shown).

Figure 2a and 2B show the dependence of the contact angle and surface tension as a function of G_a and all radii for the 2D and 3D systems, respectively. The surface tension was determined from the curvature of the interfaces, the pressures difference between the red and blue fluids and Laplace's law. The contact angle was found by calculating the angle of intersection of the fluid interface and the wall. There appears to be a slight dependence of the contact angle on the tube radius. The surface tension is constant for larger tube radii. We note that curvature cannot be determined exactly for small radii because of a limited number of pixels in the interface. In addition, wall effects may play a relatively more important role for

small radii as the effect of the fluid-fluid interaction causes a higher density of wetting fluid and a lower density of non-wetting fluid near the wall. A zero contact angle was found at G_a=0.0116 and 0.0120 for 2D and 3D systems, respectively. Corresponding lattice surface tensions were 0.165 and 0.168, respectively.

Results of the tube simulations yielded lattice capillary pressures as high as 0.11. These values allow us to conduct numerically stable LB simulations for capillary pressures between 0 and 1600 Pa (oil-water) and 0 and 2800 (air-water) for the system outlined in Table 1, well in range of the experimental conditions.
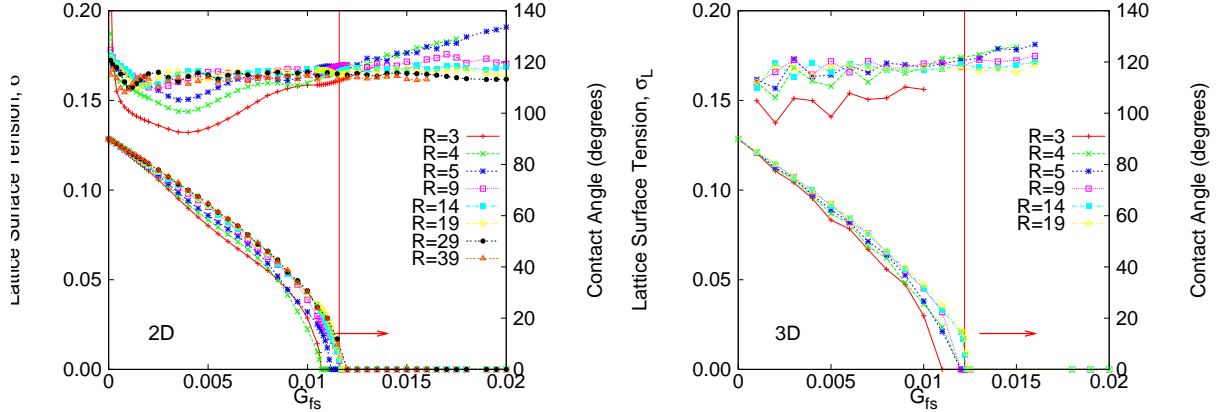
FIGURE 2. Surface tension and contact angle for 2D (left) and 3D systems (right) versus the value of the adhesion parameter, G_a, and several tube radii.

3. FLUID DISPLACEMENT SIMULATIONS POROUS MEDIA

Here we present some initial results of four displacement simulations that were carried out on porous systems described by Culligan et al. [2004, 2005]. The simulated media consist of 405x406x100 (x,y,z) voxels at the original resolution of 17e-6 m per voxel. Because of limitations in CPU time only 30% of the observed volume is studied here. The medium was filled with a wetting fluid with G_a=-0.012 and G_c=0.025. Pressure boundaries were added on top and bottom consisting of eight layers of pure fluid. The bottom boundary was filled with wetting fluid and separated from the porous media by an artificial filter consisting of alternating fluid and solid voxels (porosity=0.75). The filter served to prevent breakthrough of non-wetting fluid to the opposing boundary. The top boundary was filled with non-wetting fluid with G_a= 0.012 and G_c=0.025. The total number of nodes was approximately 2e7; simulation time was in the order of one week for 1e5 iterations on a four-CPU AMD-64 cluster.

Three simulations consisted of simple pressure steps from lattice P_c=0 to 0.038 (for a total of 1e5 iterations), 0.053 (2e5 iterations) and 0.068 (4e5 iterations). The fourth simulation consisted of five consecutive pressure steps every 1e5 iterations from P_c=0 to 0.008, 0.023, 0.038, 0.053, and 0.068 (this simulation was still ongoing at the time of writing). Figure 3 shows the saturation of the porous medium versus iterations (time) for each of the four simulations. We note here that while equilibrium can be reached within 1e5 iterations for the lower pressures (0.008, 0.023, 0.038), more than 2e5 or 4e5 iterations are needed for P_c=0.053 and 0.068, respectively. No equilibrium saturation was reached for these pressures. We also note that a cluster reboot was needed during the P_c=0.038 step for the multi-step simulation and that subsequent restart (arrow) of the simulation resulted in more drainage (i.e. lower

saturation) than expected from the results for the single step simulation for P_c=0.038. A better restart procedure was possible for the single step simulation at 2e5 iterations for P_c=0.068.

Figure 4 shows vertical saturation profiles for the P_c=0.038 and 0.068 single step simulations; the vertical porosity profile (blue) is also shown. Saturation contours are shown in increments of 2e4 iterations with each 1e5 iterations marked with thick red lines. An interesting feature in these figures is that the saturation profiles are not uniform. For the P_c=0.038 simulation it is evident that the non-wetting fluid fails to percolate beyond a depth of -90 pixels – even though this simulation attained equilibrium at the 1e5 iteration endpoint. A surprisingly low saturation is reached near the top of the sample, which is caused by the presence of wetting-non wetting interfaces at all pore entries on the top of the sample. The P_c=0.068 simulation is still not in equilibrium at 4e5 iterations -as also suggested bu the contours for 4.2e5 and 4.4e5 iterations. It appears that a more or less "uniform" saturation profile exists between a depth of -10 and -80 with the noteworthy result that there appears to be little correlation with the porosity profile. Like the P_c=0.038 simulation these results are drier at the top and much wetter at the bottom. An explanation for this behaviour is that there may be regions in the porous medium that are still inaccessible to wetting or non-wetting fluids because of pore neck/body, or percolation, effects. Another explanation may be that the fluid-fluid interfaces take up space, and therefore should exhibit some spatial correlation that, depending on the interfacial curvature, could extend beyond the spatial correlation of the solid phase. We are currently working on methods to elucidate these effects as well as quantifying the effects of interfacial curvature and interfacial area.
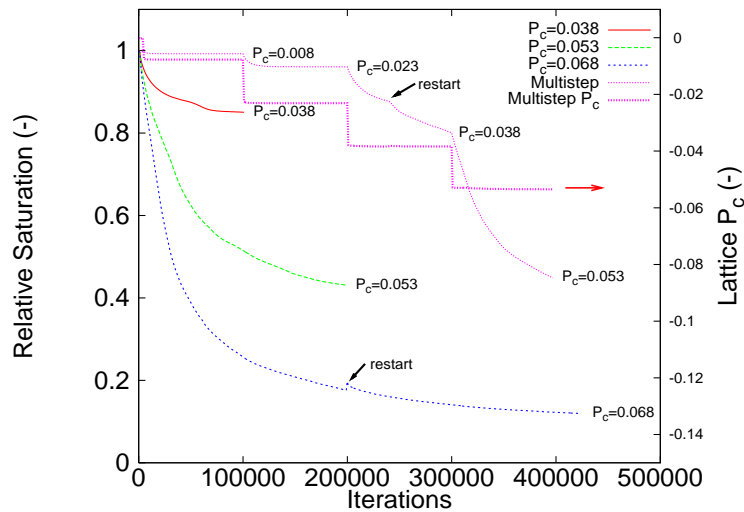

FIGURE 3. Saturation versus time (iterations) for four simulations. The pressure profile for the multi-step simulation is also shown. Because of CPU problems, two simulations were restarted at points indicated by the arrows.

4. CONCLUSION

This study provided a basic approach for the calibration of a Shan-Chen type model for simulations of wetting-non-wetting displacements in porous media. The model was subsequently applied to observed porous geometries. The current simulation results are

preliminary, but it appears that saturation profiles are not uniform near the wetting or non-wetting boundaries. This makes the subsequent analyses of the simulation results more difficult and may require even larger simulation domains before a representative elementary volume for saturation, interfacial area and curvature is obtained.
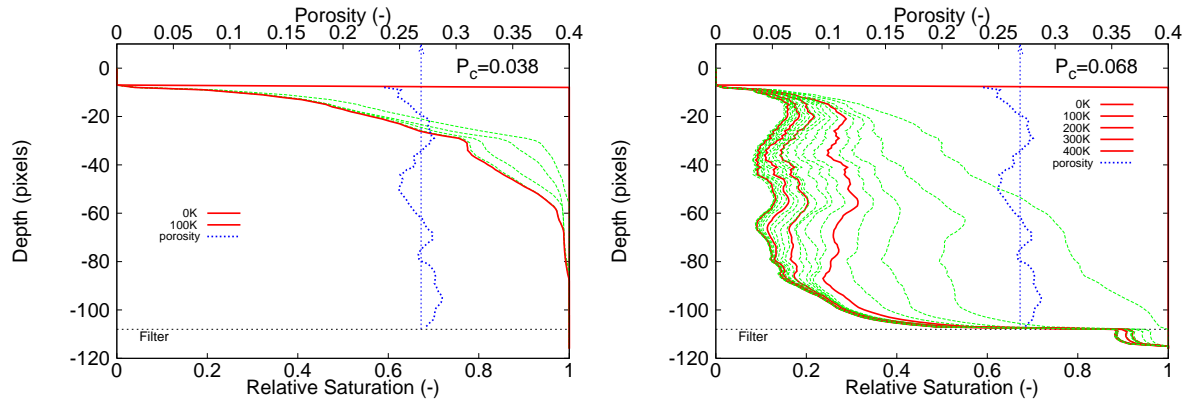

FIGURE 4. Saturation profiles for the single step simulations for P_c=0.038 and 0.068 with contours every 2e4 iterations (red lines every 1e5 iteration) the porosity profile is also shown.

Acknowledgments

References

Culligan, K.A., D. Wildenschild, B.S.B. Christensen, W.G. Gray, M.L. Rivers, and A.F.B. Tompson, 2004. *Interfacial area measurements for unsaturated flow through a porous medium*.Water Resour. Res., 40, W12413, doi:10.1029/2004WR003278.

Culligan, K.A., D. Wildenschild, B.S.B. Christensen, W.G. Gray, and M.L. Rivers, 2005. *Pore-scale characteristics of multiphase flow in porous media: a synchrotron-based CMT comparison of air-water and oil-water experiments*. Adv. Water Resour., 29, 227-238, doi:10.1016/j.adrwatres.2005.03.021.

Kechavarzi, C., K. Soga and P. Wiart, 2000. *Multispectral image analysis method to determine dynamic fluid saturation distribution in two-dimensional three-fluid phase flow laboratory experiments*. J. Contam. Hydrol., 46, 265-293.

Martys, N.S. and H. Chen, 1996. *Simulation of multicomponent fluids in complex three-dimensional geometries by the lattice Boltzmann method*. Phys. Rev. E, 53(1), 743-750.

Shan, X. and H. Chen, 1993. *Lattice Boltzmann model for simulating flows with multiple phases and components*. Phys. Rev. E, 47(3), 1815-1819.

Shan, X. and H. Chen, 1994. *Simulation of nonideal gases and liquid-gas phase transitions by the lattice Boltzmann equation*. Phys. Rev. E, 49(4), 2941-2948.

Shan, X and G. Doolen, 1996. *Diffusion in a multicomponent lattice Boltzmann equation model*. Phys. Rev. E, 54(4), 3614-3620.

Wildenschild, D., J.W. Hopmans, C.M.P. Vaz, M.L. Rivers, D. Rikard, and B.S.B. Christensen, 2002. *Using X-ray computed tomography in hydrology: systems, resolutions, and limitations*. J. Hydrol., 267(3-4), 285-297.